

# Nanopositioning System With Force Feedback for High-Performance Tracking and Vibration Control

Andrew J. Fleming, *Member, IEEE*

**Abstract**—In this study, the actuator load force of a nanopositioning stage is utilized as a feedback variable to achieve both tracking and damping. The transfer function from the applied actuator voltage to the measured load force exhibits a zero-pole ordering that greatly simplifies the design and implementation of a tracking and damping controller. Exceptional tracking and damping performance can be achieved with a simple integral controller. Other outstanding characteristics include guaranteed stability and insensitivity to changes in resonance frequency. Experimental results on a high-speed nanopositioner demonstrate an increase in the closed-loop bandwidth from 210 Hz (with an integral controller) to 2.07 kHz (with a force-feedback control). Gain margin is simultaneously improved from 5 dB to infinity.

**Index Terms**—Mechatronics, piezoelectric transducers, position control.

## I. INTRODUCTION

NANOPOSITIONING stages are used to generate fine mechanical displacements with resolution down to atomic scale [1]. Such devices include fiber aligners [2], beam scanners [3], and lateral positioning platforms [1]. Among other applications in nanotechnology [4], nanopositioning platforms are used widely in scanning probe microscopy [5]–[7] and nanofabrication systems [8]–[11]. An example of a single-degree-of-freedom lateral positioning platform is shown in Fig. 1. In this device, a force developed by a piezoelectric actuator displaces the central platform to the left.

Although piezoelectric nanopositioning systems are designed to provide the greatest possible positioning accuracy, in practice, they exhibit a number of non-ideal characteristics such as creep, hysteresis, and mechanical resonance that severely degrade the performance [1]. These characteristics are discussed in the following section. As a result of these problems, practical nanopositioning systems require position sensors and a feedback control loop to provide a satisfactory performance. The strengths and limitations of present control systems are surveyed in Section I-B.

To improve the speed and robustness of nanopositioning systems and to reduce complexity, a new control system is introduced in Section I-C. The proposed technique uses a measurement of the actuator load force to provide high-performance tracking and vibration control.

Manuscript received December 2, 2008; revised January 29, 2009 and April 22, 2009. First published October 20, 2009; current version published April 2, 2010. Recommended by Technical Editor O. Kaynak.

The author is with the School of Electrical Engineering and Computer Science, The University of Newcastle, Callaghan, N.S.W. 2308, Australia (e-mail: andrew.fleming@newcastle.edu.au).

Color versions of one or more of the figures in this paper are available online at <http://ieeexplore.ieee.org>.

Digital Object Identifier 10.1109/TMECH.2009.2028422

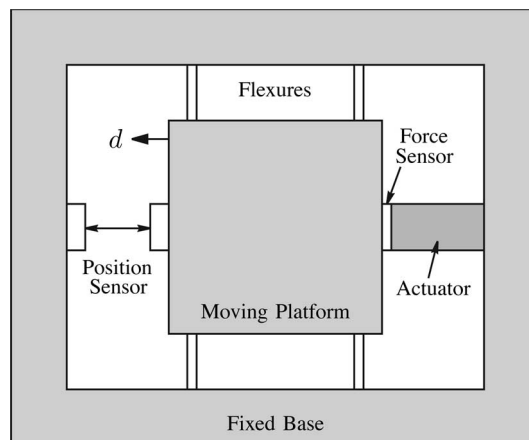


Fig. 1. Single-degree-of-freedom positioning stage. Actuator generates a force that causes the platform to displace laterally. Force sensor measures actuator load, while the position sensor measures platform displacement.

### A. Problems With Nanopositioning Systems

Due to their high stiffness, compact size, and effectively infinite resolution, piezoelectric actuators are universally employed in nanopositioning applications. The positioning accuracy of piezoelectric actuators is however severely limited by hysteresis over large displacements, and creep at low frequencies [1]. As a result, all nanopositioning systems require some form of feedback or feedforward control to reduce or eliminate non-linearity.

Another difficulty with nanopositioning systems is the mechanical resonance that arises from the platform mass interacting with the stiffness of support flexures, mechanical linkages, and actuators. As the lowest frequency resonance mode is of greatest interest, the dynamics of a nanopositioner can be approximated by a unity-gain second-order low-pass system

$$G(s) = \frac{\omega_n^2}{s^2 + 2\omega_n \xi s + \omega_n^2} \quad (1)$$

where  $\omega_n$  and  $\xi$  are the natural frequency and damping ratio. Although a second-order system is a highly simplified model, in the following, it is sufficient to demonstrate the limitations experienced by many feedback controllers. The magnitude and phase responses of this system are plotted in Fig. 2. To avoid excitation of the mechanical resonance, the frequency of driving signals is limited to between 1% and 10% of the resonance frequency (depending on the signal). In applications where the frequency of driving signals should be maximized, for example, in high-speed atomic force microscopy [12]–[15], the nanopositioner is

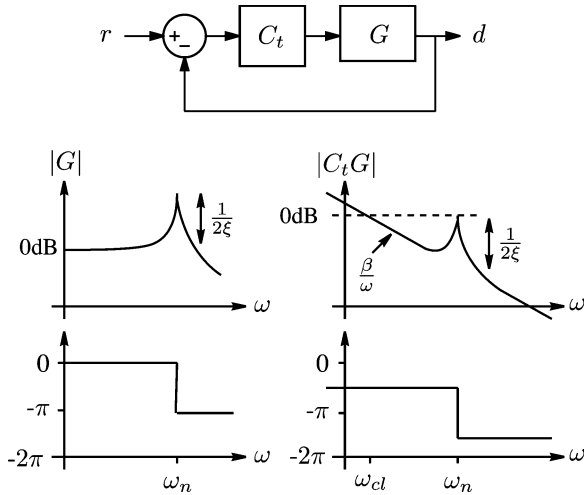


Fig. 2. Nanopositioning system  $G$  controlled by an integral controller  $C_t = \beta/s$ . Frequency response of  $G$  and system loop gain  $C_t G$  are plotted on the left- and right-hand side, respectively.

operated in open loop with driving signals that are shaped to reduce harmonic content. Although such techniques, reviewed in [16], can provide a fast response, they are not accurate as non-linearity and disturbance remain uncontrolled.

The transient response of nanopositioners can be vastly improved by actively damping the first resonance mode. This can reduce settling time by greater than 90% and allows a proportional increase in the frequency of driving signals. Systems with active damping also facilitate a greater tracking performance as the controller gain can be significantly increased; this issue is discussed in the following section.

### B. Control of Nanopositioning Systems

The most popular technique for control of commercial nanopositioning systems is sensor-based feedback using an integral or proportional–integral control [17]. Such controllers are simple, robust to modeling error, and, due to a high loop gain at low frequencies, effectively reduce piezoelectric non-linearity. However, the bandwidth of integral tracking controllers is severely limited by the presence of highly resonant modes. The cause of such a limited closed-loop bandwidth can be explained by examining the loop gain  $C_t G$  in Fig. 2. Here, the resonant system  $G$  is controlled by an integral controller  $C_t$  with gain  $\beta$ . The factor limiting the maximum feedback gain and closed-loop bandwidth is gain margin.

Above the natural frequency  $\omega_n$ , which is approximately equal to the resonance frequency in systems with low damping, the phase lag of the loop gain exceeds  $\pi$ , so the magnitude must be less than 1 (0 dB) for stability in a closed loop. The condition for closed-loop stability is approximately

$$\frac{\beta}{\omega_n} \times \frac{1}{2\xi} < 1, \text{ or } \beta < 2\omega_n\xi. \quad (2)$$

As the system  $G$  is unity gain, the complimentary sensitivity function is

$$\frac{d(s)}{r(s)} = \frac{C_t(s)G(s)}{C_t(s)G(s) + 1} \approx \frac{\beta}{s + \beta}. \quad (3)$$

Thus, the feedback gain  $\beta$  is also the approximate 3dB bandwidth of the complimentary sensitivity function  $\omega_{cl}$  and the 0 dB crossing of the loop gain (in radians per second). From this fact, and the stability condition (2), the maximum closed-loop bandwidth is equal to the product of damping ratio  $\xi$  and natural frequency  $\omega_n$ , i.e.,

$$\text{Max. closed-loop bandwidth} < 2\omega_n\xi. \quad (4)$$

This is a severe limitation as the damping ratio is usually in the order of 0.01, so the maximum closed-loop bandwidth is less than 2% of the resonance frequency.

Techniques aimed at improving the closed-loop bandwidth are based on either inversion of resonant dynamics using a notch filter [18] or damped resonant dynamics using a damping controller [19], [20].

Inversion techniques are popular as they are simple to implement and can provide an excellent closed-loop bandwidth, up to or greater than the resonance frequency [18]. The major disadvantage is the requirement for an accurate system model. If the system resonance frequency significantly decreases, a high-gain inversion-based feedback controller can become unstable. In many applications, this is unacceptable as the load mass and resonance frequency of a nanopositioner can vary significantly during service. As a result of this sensitivity, high-performance inversion-based controllers are usually applied in applications where the resonance frequency is stable, or where the feedback controller can be continually recalibrated [18].

Damping control is an alternative method for reducing the bandwidth limitations imposed by mechanical resonance. Damping control uses a feedback loop to artificially increase the damping ratio  $\xi$  of a system. Due to (4), an increase in  $\xi$  allows a proportional increase in the feedback gain and closed-loop bandwidth. Although damping controllers alone cannot increase the closed-loop bandwidth to beyond the resonance frequency, they have the advantage of being insensitive to variations in resonance frequency. In addition, as damping controllers suppress, rather than invert, the mechanical resonance, they provide better rejection of external disturbances than inversion-based systems [1].

A number of techniques for damping control have been demonstrated successfully in the literature, these include positive position feedback (PPF) [21], polynomial based control [20], shunt control [22], [23], resonant control [24], and integral resonant control (IRC) [19], [25], [26]. These techniques can successfully damp a resonant system with modest insensitivity to variations in the resonance frequency. However, when the damped system is included in an integral tracking loop, the system is still limited by a low gain margin. In addition, the wide bandwidth of a damping controller can introduce a significant amount of sensor-induced positioning noise, which cannot be reduced in the normal way by scaling back the tracking controller gain.

To demonstrate the limitations imposed by sensor noise, consider a nanopositioner with feedback control derived from a high-performance capacitive sensor with a range of  $\pm 100 \mu\text{m}$  and root-mean-square (RMS) noise density of  $20 \text{ pm}/\sqrt{\text{Hz}}$ . An estimate of the RMS positioning noise can be found by multiplying the noise density by the square root of the closed-loop bandwidth, i.e.,

$$\text{RMS noise} = \sqrt{2 \times \text{bandwidth} \times \text{noise density}}. \quad (5)$$

For example, with a closed-loop bandwidth of 100 Hz, the positioning noise is 0.28 nm RMS. If the noise is normally distributed, the RMS value is also the standard deviation  $\sigma$ . As the peak-to-peak amplitude of a Gaussian process in  $6\sigma$ , the noise will be approximately 1.7 nm peak-to-peak. For atomic resolution, the closed-loop bandwidth must be reduced to below 1 Hz, a severe limitation.

At this point in the discussion, it should be noted that feedforward control can be employed to improve the performance of feedback-controlled nanopositioning systems [27]–[29]. Although feedforward techniques can also be used independently [30], they are generally combined with a feedback controller to ensure some immunity to modeling error, drift, and external disturbances. The foremost benefit resulting from the addition of a feedforward controller is the increased tracking performance that arises from a partial inversion of the closed-loop dynamics. However, as the non-linearity, bandwidth, and resolution of a nanopositioning system are limited primarily by the feedback controller, improving the feedback system is of primary concern. Furthermore, if a nanopositioner can experience significant changes in resonance frequency, feedforward control may not be feasible [31].

If the reference signal is periodic, iterative feedforward control [32], [33] and adaptive control [34] can be applied. These techniques can provide excellent tracking performance at high speed, but require a periodic input and significant digital signal processing capabilities.

### C. Contribution of This Work

From the previous discussion, it should be clear that tracking controllers can provide good performance at low frequencies; however, the maximum gain and closed-loop bandwidth are severely limited by the presence of a lightly damped mechanical resonance. As discussed, damping controllers can provide a substantial improvement, but the tracking controller bandwidth is still restricted by low stability margins. A further limitation of present techniques is the high sensor-induced noise that places a penalty on positioning resolution as bandwidth is increased.

In this study, a new method for feedback control of nanopositioning systems is proposed. A measurement of the force applied to the moving platform by the actuator is utilized as a feedback variable for both tracking and damping control. A major benefit of this arrangement is discussed in Section II. The system exhibits a zero-pole ordering, meaning that the resonant zeros of the system appear lower in frequency than the resonant poles. Section II also presents a new modeling technique for piezoelectric actuators. Rather than modeling piezoelectric actuators

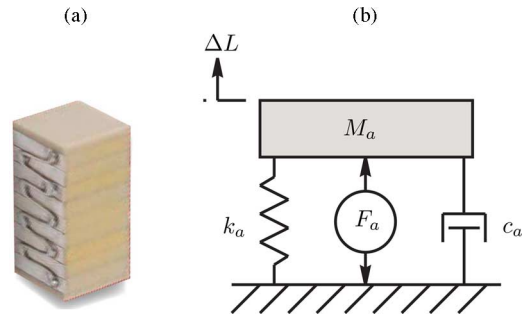


Fig. 3. (a) Noliac monolithic stack actuator represented in (b) by a voltage dependent force  $F_a$ , stiffness  $k_a$ , effective mass  $M_a$ , and damping coefficient  $c_a$ .

as displacement actuators, they are modeled as force actuators. This technique provides a more intuitive understanding of actuator dynamics and is simpler to apply.

In Section III, the unique properties of the system described in Section II are exploited to provide damping control. A simple integral controller is shown to provide damping performance without any limitations on the gain. The system is guaranteed to be stable with a theoretically infinite gain margin and  $90^\circ$  phase margin.

In addition to damping control, the controller described in Section III is extended to provide tracking control without loss of performance or stability margins. As the noise generated by a piezoelectric force sensor is much less than a capacitive or inductive position sensor, the closed-loop positioning noise is also substantially reduced. The performance of the proposed techniques are demonstrated experimentally in Section V.

The increased bandwidth and resolution offered by the proposed technique, combined with the simple implementation and high level of robustness, will allow nanopositioning systems to be employed in a new range of high-speed applications. For example, due to the performance penalties associated with closed-loop control, high-speed scanning probe microscopes currently use open-loop nanopositioners [12]–[15]. Due to the simplicity and bandwidth of the proposed technique, such applications can now utilize closed-loop control with the associated benefits of improved linearity, less vibration, and rejection of disturbance.

## II. MODELING

In this section, a model is derived for the single-degree-of-freedom lateral positioning platform illustrated in Fig. 1. In this device, the force developed by a piezoelectric actuator displaces the central platform. The flexures represent the stiffness introduced by guiding flexures and mechanical linkages that are often present between the actuator and platform. Although the model presented is simple, it adequately represents the dominant dynamics exhibited by many nanopositioning geometries.

### A. Actuator Dynamics

A typical multilayer monolithic stack actuator is shown in Fig. 3(a). The actuator experiences an internal stress in response

to an applied voltage. This stress is represented by the voltage dependent force  $F_a$  and is related to free displacement by

$$\Delta L = \frac{F_a}{k_a} \quad (6)$$

where  $\Delta L$  is the change in actuator length (in meter) and  $k_a$  is the actuator stiffness (in N/m).

The developed force  $F_a$  is most easily related to applied voltage by beginning with the standard expression for unrestrained linear stack actuators [35],

$$\Delta L = d_{33} n V_a \quad (7)$$

where  $d_{33}$  is the piezoelectric strain constant (in m/V),  $n$  is the number of layers, and  $V_a$  is the applied voltage. Combining (6) and (7) yields an expression for developed force as a function of applied voltage

$$F_a = d_{33} n k_a V_a. \quad (8)$$

The force equation can also be derived from the stress-charge form of the piezoelectric constituent equations [36]

$$T = d_{33} c^E E \quad (9)$$

where  $T$  is the stress (in N/m<sup>2</sup>),  $c^E$  is Young's elastic modulus under constant electric field (in N/m<sup>2</sup>), and  $E$  is the applied electric field (in V/m). The developed force  $F_a$  is proportional to stress  $T$  and the surface area  $A$  (in m<sup>2</sup>) by  $F_a = TA$ . Also, the electric field is equal to the applied voltage  $V_a$  divided by the layer thickness  $t$ , i.e.,  $E = V_a/t$ . Taking this into account, the developed force is

$$F_a = \frac{d_{33} c^E A V_a}{t}. \quad (10)$$

This can be simplified by recognizing that the number of layers  $n$  is equal to the length  $L$  divided by layer thickness  $t$ , i.e.,  $n = L/t$ . The elasticity  $c^E$  can also be replaced by stiffness, which is related to elasticity by

$$k_a = \frac{c^E A}{L}. \quad (11)$$

The resulting expression for the developed force is again

$$F_a = d_{33} n k_a V_a. \quad (12)$$

That is, the ratio of the developed force to applied voltage is  $d_{33} n k_a$  N/V. In the following sections, this constant will be denoted by  $g_a$  where

$$F_a = g_a V_a \quad \text{and} \quad g_a = d_{33} n k_a.$$

Compared to standard modeling techniques [35], which are based on displacement, the method described earlier results in an expression for generated force. This approach provides an intuitive understanding of the actuator mechanics and significantly simplifies the modeling of interconnected structures such as nanopositioners as the generated actuator force is independent of load force and stiffness. The ease of combining the actuator and structural models when using developed force rather than displacement will become clear in Section II-D.

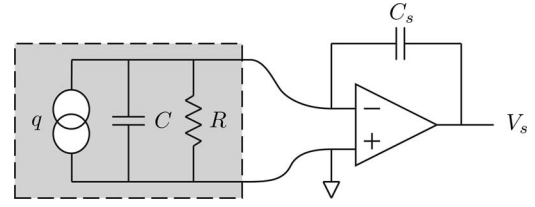


Fig. 4. Electrical model of a piezoelectric force sensor is shown in gray. Developed charge  $q$  is proportional to the strain and hence the force experienced by the sensor. Op-amp charge amplifier produces an output voltage  $V_s$  equal to  $-q/C_s$ .

## B. Sensor Dynamics

Although the load force  $F_s$  can be measured in a number of ways, in this application it is desirable to minimize the additional mass and compliance associated with the sensor. In such scenarios, piezoelectric transducers are an excellent choice. They provide a high sensitivity and bandwidth with low noise at high frequencies.

If a single wafer of piezoelectric material is sandwiched between the actuator and platform, the amount of generated charge per unit area  $D$  (in C/m<sup>2</sup>) is given by the standard strain-charge form of the piezoelectric constituent equations [36]

$$D = d_{33} T. \quad (13)$$

The generated charge is then

$$q = d_{33} F_s. \quad (14)$$

If an  $n$ -layer piezoelectric transducer is used as a force sensor, the generated charge is

$$q = n d_{33} F_s. \quad (15)$$

The electrical model of a piezoelectric force sensor and charge measurement circuit is shown in Fig. 4. In this circuit, the output voltage  $V_s$  is equal to

$$V_s = -\frac{q}{C_s} = -\frac{n d_{33} F_s}{C_s} \quad (16)$$

that is, the scaling between the force and voltage is  $-\frac{n d_{33}}{C_s}$  V/N.

Piezoelectric force sensors can also be calibrated using voltage rather than charge measurement. In this case, the generated charge is deposited on the transducer's internal capacitance. As the terminal voltage is non-zero, the dynamics of the sensor are slightly altered. In effect, the transducer is marginally stiffened [37]. However, as the stiffness of the sensor is already substantially greater than that of the actuator and flexures, this effect is negligible. The open-circuit voltage of a piezoelectric force sensor is

$$V_s = \frac{n d_{33} F_s}{C} \quad (17)$$

where  $C$  is the transducer capacitance defined by  $C = n \epsilon_T A/h$ , and  $A$ ,  $h$ , and  $\epsilon_T$  are the area, layer thickness, and dielectric permittivity under a constant stress. The scaling factor between force and measured voltage is  $\frac{n d_{33}}{C}$  V/N. In the following

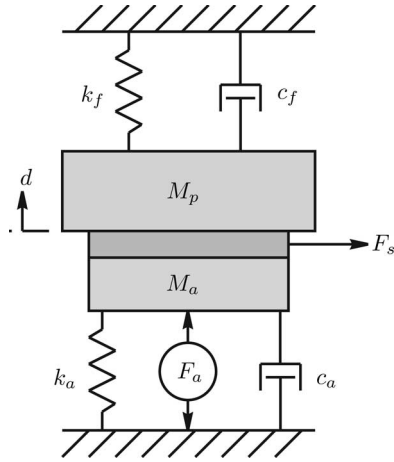


Fig. 5. Mechanical diagram of a single-degree-of-freedom positioning stage.  $F_s$  is the measured force acting between the actuator and platform mass in the vertical direction.

sections, this sensor constant will be denoted by  $g_s$ , i.e.,

$$V_s = g_s F_s \quad \text{and} \quad g_s = \frac{nd_{33}}{C}. \quad (18)$$

### C. Sensor Noise

Due to the high mechanical stiffness of piezoelectric force sensors, thermal or the Boltzmann noise is negligible compared to the electrical noise arising from interface electronics. As piezoelectric sensors have a capacitive source impedance, the sensor noise density  $N_{V_s}(\omega)$  is due primarily to current noise  $i_n$  reacting with the capacitive source impedance, i.e.,

$$N_{V_s}(\omega) = i_n \frac{1}{C\omega} \quad (19)$$

where  $N_{V_s}$  and  $i_n$  are the power spectral densities, measured in V and  $A/\sqrt{\text{Hz}}$ , respectively. Note that the high-pass filter arising from the transducer's leakage resistance has been ignored, as this pole is approximately canceled by the  $1/f$  corner frequency<sup>1</sup> of the current noise density  $i_n$  [39].

In addition to noise, piezoelectric force sensors also exhibit other non-ideal characteristics. These include temperature dependence and a small amount of non-linearity. A thorough treatment of these topics is beyond the scope of this paper. However, if such characteristics must be avoided, dedicated piezoelectric sensor compositions are available with extremely high linearity and essentially no temperature dependence, e.g., quartz or gallium phosphate.

### D. Mechanical Dynamics

The mechanical diagram of a single axis positioner is shown in Fig. 5. The developed actuator force  $F_a$  results in a load force  $F_s$  and platform displacement  $d$ . The stiffness and damping coefficient of the flexures and actuator are denoted by  $k_f$ ,  $c_f$ , and  $k_a$ ,  $c_a$ , respectively.

<sup>1</sup>The power spectral density of an electronic device is approximately constant above the  $1/f$  corner frequency, while below this frequency, it is approximately proportional to the inverse of frequency [38].

The dynamics of the suspended platform are governed by Newton's second law,

$$(M_a + M_p)\ddot{d} = F_a - k_a d - k_f d - c_a \dot{d} - c_f \dot{d} \quad (20)$$

where  $M_a$  and  $M_p$  are the effective mass of the actuator and the mass of the platform. As the actuator and flexure are mechanically in parallel with the suspended platform, the masses, stiffness, and damping coefficients can be grouped together, i.e.,

$$M = M_a + M_p \quad (21)$$

$$k = k_a + k_f \quad \text{and} \quad (22)$$

$$c = c_a + c_f.$$

The equation of motion is then

$$M\ddot{d} + kd + c\dot{d} = F_a \quad (23)$$

and the transfer function from actuator force  $F_a$  to platform displacement  $d$  is

$$\frac{d}{F_a} = \frac{1}{Ms^2 + cs + k}. \quad (24)$$

Including the actuator gain, the transfer function from applied voltage to displacement can be written as

$$G_{dV_a} = \frac{d}{V_a} = \frac{g_a}{Ms^2 + cs + k}. \quad (25)$$

The load force  $F_s$  is also of interest; this can be related to the actuator force  $F_a$  by applying Newton's second law to the actuator mass,

$$M_a \ddot{d} = F_a - k_a d - c_a \dot{d} - F_s. \quad (26)$$

This results in the following transfer function between the applied force  $F_a$  and measured force  $F_s$ :

$$\frac{F_s}{F_a} = 1 - (M_a s^2 + c_a s + k_a) \frac{d}{F_a} \quad (27)$$

$$= \frac{M_p s^2 + c_f s + k_f}{Ms^2 + cs + k}. \quad (28)$$

By including the actuator and sensor gains  $g_a$  and  $g_s$ , the system transfer function from the applied voltage to the measured voltage can be found:

$$G_{V_s V_a} = \frac{V_s}{V_a} = g_a g_s \frac{M_p s^2 + c_f s + k_f}{Ms^2 + cs + k}. \quad (29)$$

The two system transfer functions  $G_{dV_a}$  and  $G_{V_s V_a}$  will be used in the following sections to simulate the performance of feedback control systems. As both of these transfer functions have the same input  $V_a$  and poles, it is convenient to define a single-input two-output system  $G$  that contains both of these transfer functions

$$G = \begin{bmatrix} G_{dV_a} \\ G_{V_s V_a} \end{bmatrix}. \quad (30)$$

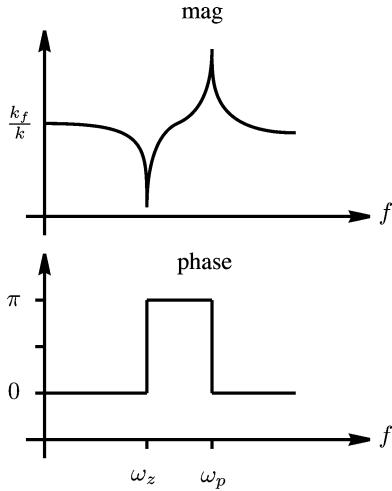


Fig. 6. Magnitude and phase response of  $F_s/F_a$  (27).

### E. System Properties

The transfer function  $G_{V_s V_a}$  (29) can be rewritten as

$$G_{V_s V_a} = g_a g_s \frac{M_p}{M} \frac{s^2 + \frac{c_f}{M_p} s + \frac{k_f}{M_p}}{s^2 + \frac{c}{M} s + \frac{k}{M}}. \quad (31)$$

This transfer function consists of a pair of resonant poles and zeros at frequencies  $\omega_z$  and  $\omega_p$ ,

$$\omega_z = \sqrt{\frac{k_f}{M_p}} \quad \omega_p = \sqrt{\frac{k}{M}} = \sqrt{\frac{k_a + k_f}{M_a + M_p}}.$$

In general, the resonance frequency of the zeros will appear below the poles. The condition for this to occur is

$$\begin{aligned} \omega_z &< \omega_p \\ \frac{k_f}{M_p} &< \frac{k_a + k_f}{M_a + M_p} \\ M_a k_f &< k_a M_p. \end{aligned} \quad (32)$$

As the actuator mass  $M_a$  and flexural stiffness  $k_f$  are significantly less than the actuator stiffness  $k_a$  and platform mass  $M_p$ , the resonant zeros will always occur below the resonance frequency of the poles. This characteristic is shown in the frequency response of  $F_s/F_a$  in Fig. 6.

### F. Example System

For the sake of demonstration, and to assess the validity of assumptions in the following sections, an example system will be considered. The system is a single-dimensional positioning stage as illustrated in Figs. 1 and 5. The actuator is a 10-mm long PZT linear actuator with 200 layers. Force sensing is provided by a single PZT wafer of the same area. The dimensions and physical properties of the system are listed in Table I.

The actuator and sensor gains are

$$g_a = 7.5 \text{ N/V} \quad \text{and} \quad g_s = 0.19 \text{ V/N} \quad (33)$$

TABLE I  
EXAMPLE SYSTEM PARAMETERS

Parameter	Symbol	Value
Platform Mass	$M_p$	100 g
Actuator Mass	$M_a$	2 g
Actuator Area	$A$	5×5 mm
Actuator Length	$L$	10 mm
Young's Modulus	$c^E$	50 GPa
Charge Constant	$d_{33}$	300×10 <sup>-12</sup> C/N
Actuator Stiffness	$k_a$	125 N/μm
Flexure Stiffness	$k_f$	50 N/μm
Actuator Layers	$n$	200
Actuator Damping	$c_a$	100 N/ms <sup>-1</sup>
Flexure Damping	$c_f$	100 N/ms <sup>-1</sup>

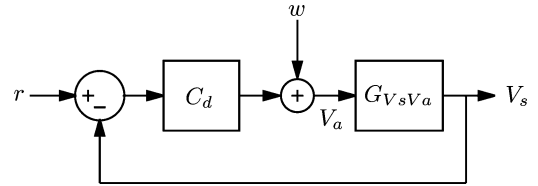


Fig. 7. Nanopositioning system  $G_{V_s V_a}$  with input and output voltages  $V_a$  and  $V_s$  proportional to applied and measured forces, controlled by an IFF damping controller  $C_d(s)$ .

which results in an open-loop static displacement sensitivity  $G_{dV_a}(0)$  of

$$G_{dV_a}(0) = \frac{g_a}{k} = 43 \text{ nm/V}. \quad (34)$$

The full scale displacement is 8.5 μm at 200 V, and the system resonance frequencies are

$$\omega_p = 6.3 \text{ kHz} \quad \text{and} \quad \omega_z = 3.6 \text{ kHz}. \quad (35)$$

The open-loop frequency response is plotted in Fig. 9.

### III. DAMPING CONTROL

The technique of integral force feedback (IFF) has been widely applied for augmenting the damping of flexible structures [40]–[42]. The feedback law is simple to implement and, under common circumstances, provides excellent damping performance with guaranteed stability [41]. In the following, IFF is applied to augment the damping of nanopositioning systems.

The feedback diagram of an IFF damping controller is shown in Fig. 7.

A key observation of the system  $G_{V_s V_a}$  is that its phase response lies between 0 and 180°. This is a general feature of flexible structures with inputs and outputs proportional to applied and measured forces [41]. A unique property of such systems is that integral control can be directly applied to achieve damping, i.e.,

$$C_d(s) = \frac{\alpha}{s} \quad (36)$$

where  $\alpha$  is the controller gain. As the integral controller has a constant phase lag of 90°, the loop-gain phase lies between -90 and 90°. That is, the closed-loop system has an infinite gain margin and phase margin of 90°. Simplicity and robustness are two outstanding properties of systems with IFF.

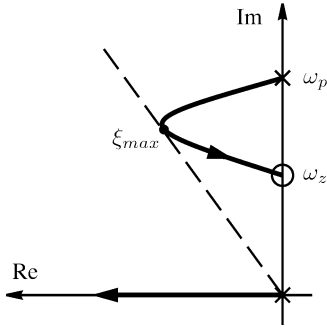


Fig. 8. Root locus of a nanopositioning system  $G_{V_s V_a}$  with integral damping controller  $C_d$ .

A solution for the optimal feedback gain  $\alpha$  has already been derived in [41]. These results can be directly adapted for the system considered in this study. The method makes the valid assumption that system damping coefficients are small and can be neglected. A further valid simplification is that the actuator mass  $M_a$  is negligible compared to the platform mass  $M_p$ . With these assumptions, the optimal feedback gain  $\alpha^*$  and the corresponding maximum closed-loop damping ratio  $\xi^*$  are

$$\alpha^* = \frac{\omega_p \sqrt{\omega_p / \omega_z}}{g_s g_a} \quad (37)$$

and

$$\xi^* = \frac{\omega_p - \omega_z}{2\omega_z} \quad (38)$$

An expression for the closed-loop poles can also be adapted from [41]. The closed-loop poles are given by the roots of the following equation:

$$1 + \alpha g_s g_a \frac{s^2 + \omega_z^2}{s(s^2 + \omega_p^2)} = 0. \quad (39)$$

The corresponding closed-loop root locus is plotted in Fig. 8 [41]. Note that the closed-loop poles remain in the left-half plane and that the system is unconditionally stable. The root locus also provides a straightforward method for finding the optimal feedback gain numerically. This can be useful if the model parameters are unknown, i.e., if the system  $G_{V_s V_a}$  was procured directly from experimental data by system identification. This approach is discussed in Section V.

For the example system described in Section II-F, the optimal gain and maximum damping ratio are computed from (37) and (38), the result is

$$\alpha^* = 4.0 \times 10^4 \quad \text{and} \quad \xi^* = 0.43. \quad (40)$$

These values can be checked with a numerical root-locus plot. The numerically optimal gain is  $4.07 \times 10^4$  which provides a closed-loop damping ratio of 0.45. This correlates closely with the predicted values and supports the accuracy of the assumptions made in deriving the optimal gain.

The simulated open- and closed-loop frequency responses from the disturbance input  $w$  to the measured sensor voltage  $V_s$  are plotted in Fig. 9. Clearly the controller significantly im-

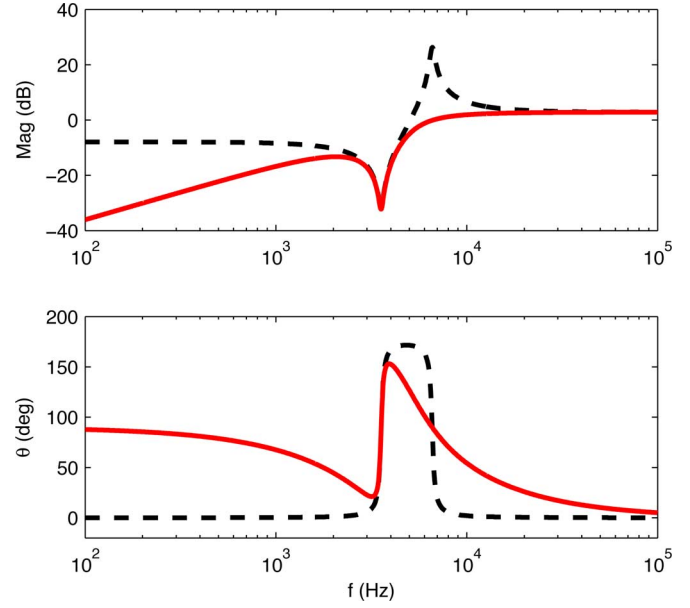


Fig. 9. Open-loop (dashed line) and closed-loop (solid line) frequency response from  $w$  to  $V_s$ .

proves the system damping and disturbance rejection at low frequencies.

#### IV. TRACKING CONTROL

After studying the relationship between force and displacement in the following section, three different tracking controller architectures will be discussed.

##### A. Relationship Between Force and Displacement

The relationship between measured force and displacement can be found either by applying Newton's second law to the platform mass or by multiplying the two system transfer functions (24) and (27), i.e.,

$$\frac{d}{F_s} = \frac{d}{F_a} \left( \frac{F_s}{F_a} \right)^{-1} \quad (41)$$

$$\frac{d}{F_s} = \frac{1}{M_p s^2 + c_f s + k_f}. \quad (42)$$

Thus, the measured voltage  $V_s$  is related to displacement by

$$\frac{d}{V_s} = \frac{d}{g_s F_s} = \frac{1/g_s}{M_p s^2 + c_f s + k_f}. \quad (43)$$

From the transfer function  $d/V_s$  (43), it can be observed that displacement is proportional to force up until the frequency of the system zeros,  $\omega_z = \sqrt{k_f/M_p}$ . The scaling factor is  $g_{cl} = 1/g_s k_f$  m/V. That is,

$$d \approx g_{cl} V_s = \frac{1}{g_s k_f} V_s \quad \omega < \omega_z. \quad (44)$$

Above  $\omega_z$ , the measured force and voltage are proportional to platform acceleration. The scaling factor is  $1/g_s M_p$  ms<sup>-2</sup>/V.

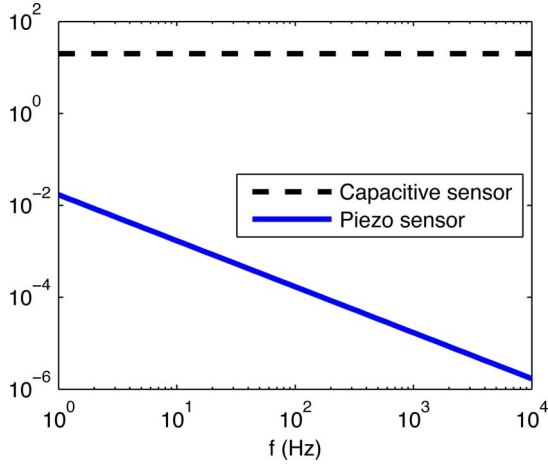


Fig. 10. Simulated position noise spectral density (in picometres/ $\sqrt{\text{Hz}}$ ) of a state-of-the-art capacitive sensor and the piezoelectric force sensor described in Section II-F.

That is,

$$ds^2 \approx \frac{1}{g_s M_p} V_s \quad \omega > \omega_z. \quad (45)$$

As  $V_s$  is directly proportional to displacement at frequencies below  $\omega_z$ , it makes an excellent feedback variable when trajectory tracking is required.

A key benefit of using the piezoelectric force sensor is its extremely low noise density. The approximate position noise density  $N(\omega)$  can be found by combining (19) and (44),

$$N(\omega) = i_n \frac{1}{C\omega} \frac{1}{g_s k_f} \quad (46)$$

where  $i_n$  is the current noise density of the interface electronics and  $C$  is the sensor capacitance. The position noise density of the example system is compared to the noise density of a state-of-the-art capacitive sensor (20 pm/ $\sqrt{\text{Hz}}$ ) in Fig. 10. The plot demonstrates the extremely low position noise of the piezoelectric sensor. This simulation uses the current noise density from a general purpose LM833 FET-input op-amp, which is 0.5 pA/ $\sqrt{\text{Hz}}$ .

In following sections,  $N_{V_s}(\omega)$  and  $N_d(\omega)$  will be used to represent the additive sensor noise exhibited by the piezoelectric voltage measurement and capacitive displacement sensor.

### B. Integral Displacement Feedback

The most straightforward technique for achieving displacement tracking is to simply enclose the system in an integral feedback loop, as depicted in Fig. 11(a). The tracking controller  $C_t$  is simply

$$C_t = \frac{\beta}{s}. \quad (47)$$

In this strategy, the displacement  $d$  must be obtained with a physical displacement sensor such as a capacitive, inductive, or optical sensor [43].

As discussed in Section I, the foremost limitation of integral tracking controllers is the low gain margin. For the example system, the bandwidth is limited to only 60 Hz with a 5-dB gain margin. The gain margin is also highly sensitive to variations in resonance frequency.

### C. Direct Tracking Control

The low bandwidth of integral tracking controllers can be significantly improved by adding an internal force-feedback loop as shown in Fig. 11(b). As the damping controller eliminates the lightly damped resonance, the gain margin is drastically increased, allowing a proportional increase in tracking bandwidth. This was discussed in Section I-A.

To find the closed-loop transfer function, it is first convenient to find the transfer function of the internal loop. That is, the transfer function  $\widehat{G}_{du}$  from  $u$  to  $d$ , which is

$$\widehat{G}_{du} = \frac{G_{dV_a} C_d}{1 + C_d G_{V_s V_a}}. \quad (48)$$

The closed-loop response  $\widehat{G}_{dr}$  from  $r$  to  $d$  is then

$$\widehat{G}_{dr} = \frac{C_t \widehat{G}_{du}}{1 + C_t \widehat{G}_{du}} \quad (49)$$

or equivalently,

$$\widehat{G}_{dr} = \frac{G_{dV_a} C_t C_d}{1 + G_{dV_a} C_t C_d + C_d G_{V_s V_a}}. \quad (50)$$

The frequency response of this transfer function is plotted in Fig. 11(b). Compared to the integral controller with the same gain margin (5 dB), the bandwidth has been increased from 60 Hz to 1 kHz. Although this is an excellent improvement, the gain margin is still sensitive to changes in resonance frequency. In practice, the controller needs to be conservatively designed for stability with the lowest possible resonance frequency.

One disadvantage of increasing closed-loop bandwidth is that position noise is increased. This is illustrated by the wider bandwidth power spectral density plotted in Fig. 11(b). The closed-loop power spectral density  $\widehat{N}_d(\omega)$  is obtained from the density of additive sensor noises,  $N_d(\omega)$  and  $N_{V_s}(\omega)$ , and the noise sensitivity of the control loop. As the piezoelectric sensor noise  $N_{V_s}(\omega)$  is negligible compared to  $N_d(\omega)$ ,  $\widehat{N}_d(\omega)$  can be approximated by

$$\widehat{N}_d(\omega) = \left| \frac{-G_{dV_a} C_t C_d}{1 + G_{dV_a} C_t C_d + C_d G_{V_s V_a}} \right| N_d(\omega). \quad (51)$$

### D. Dual-Sensor Feedback

In Section IV-A, it was found that measured force is proportional to displacement at frequencies below the system zeros. A logical progression is to simply apply a reference input  $r$  to the force-feedback loop and expect displacement tracking at frequencies from DC to  $\omega_z$ . Unfortunately this is not possible due to the high-pass filter formed by the piezoelectric capacitance and finite input impedance of charge amplifiers and voltage buffers.

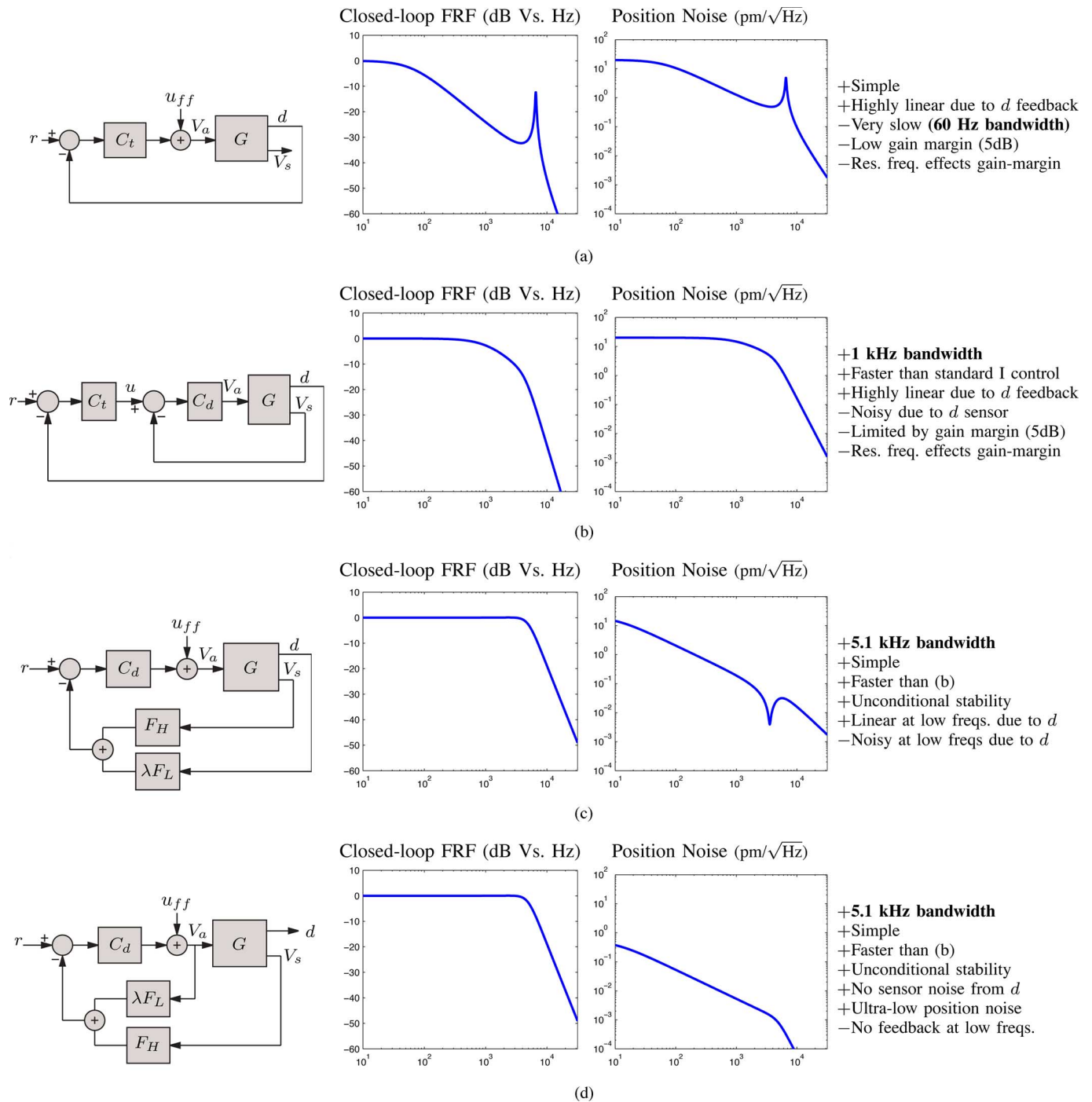


Fig. 11. Comparison of basic integral control, force-feedback and direct tracking control, force-feedback control with dual sensors, and force-feedback control with low-frequency bypass. Closed-loop frequency responses are measured from the applied reference to the resulting displacement in  $\mu\text{m}$ . (a) Basic integral control. (b) Direct tracking control. (c) Dual-sensor feedback. (d) Low-frequency bypass.

The measured voltage across a piezoelectric sensor is equal to

$$V_s = V_p \frac{s}{s + 1/R_{in}C} \quad (52)$$

where  $V_p$  is the piezoelectric strain voltage,  $R_{in}$  is the voltage buffer input impedance, and  $C$  is the transducer capacitance. The filter is high pass with a cut-off frequency of  $1/R_{in}C$ .

Although the high-pass cut-off frequency can be made extremely low, in the order of 1 mHz, this is not desirable as the

settling time becomes extremely long. A preferable solution is to use the displacement measurement  $d$  at low frequencies where the piezoelectric force sensor is inaccurate.

The diagram of a dual-sensor control loop is shown in Fig. 11(c). This tracking control loop is similar to Fig. 7 except for the additional complementary filters  $F_H$  and  $F_L$ . These complementary filters substitute the displacement measurement  $d$  for  $V_s$  at frequencies below the crossover frequency  $\omega_c$ , which in this study is 10 Hz. The simplest choice of complementary

filters are

$$F_H = \frac{s}{s + \omega_c} \quad \text{and} \quad F_L = \frac{\omega_c}{s + \omega_c}. \quad (53)$$

As the measured displacement signal  $d$  will have a different sensitivity than  $V_s$ , it must be scaled by an equalizing constant  $\lambda$ , as shown in the diagram. The value of  $\lambda$  should be

$$\lambda = \frac{G_{VsVa}(0)}{G_{dVa}(0)}. \quad (54)$$

If  $\lambda$  is chosen correctly, the closed-loop response  $\widehat{G}_{dr}$  is

$$\widehat{G}_{dr} = \frac{G_{dVa}C_d}{1 + C_dG_{VsVa}}. \quad (55)$$

As this control loop is unconditionally stable, there is no restriction on the gain of  $C_d$ . However,  $C_d$  was chosen in the previous section to provide an optimal damping performance, this value should be retained. Further increases in  $C_d$  are not productive as the disturbance rejection at the resonance frequency will degrade.

The higher gain of the force-feedback loop provides an increase in bandwidth from 1 to 5.1 kHz compared to the direct tracking controller discussed in the previous section. This increase also comes with a theoretically infinite gain margin and 90° phase margin, both of which are immune to variations in resonance frequency.

The closed-loop position noise density of the dual-sensor controller is given by

$$\widehat{N}_d(\omega) = \left| \frac{-F_L G_{VsVa} C_d}{1 + G_{VsVa} C_d} \right| N_d(\omega). \quad (56)$$

Analogous to the direct tracking controller, position noise due to the piezoelectric force sensor is negligible and can be neglected. As the displacement sensor noise is now filtered by  $F_L$ , a significant improvement in noise performance is achieved. This is plotted in Fig. 11(c).

Although physical displacement sensors are much noisier than piezoelectric transducers, they also have better linearity and lower drift [39]. The complementary filters  $F_H$  and  $F_L$  exploit the best aspects of each signal. The wide bandwidth and low noise of piezoelectric force sensors are exploited above the crossover frequency  $\omega_c$ , while the physical displacement sensors provide a high level of thermal stability at DC and below the crossover frequency  $\omega_c$ .

### E. Low-Frequency Bypass

If a physical displacement sensor is not available, or the system does not require a high level of DC accuracy, the low frequency displacement can be estimated from the input voltage  $V_a$  as shown in Fig. 11(d). This scheme can be viewed as a simple first-order observer that estimates DC position. The signal  $V_a$  requires the same sensitivity as  $V_s$ , so the scaling constant  $\lambda$  is

$$\lambda = G_{VsVa}(0). \quad (57)$$

If  $\lambda$  is chosen correctly, the closed-loop response and stability characteristics are the same as that discussed in the previous

section. The foremost benefit of eliminating the physical displacement sensor is noise reduction. The closed-loop position noise density, plotted in Fig. 11(d), is now

$$\widehat{N}_d(\omega) = \left| \frac{-F_H G_{dVa} C_d}{1 + G_{VsVa} C_d} \right| N_{Vs}(\omega) \quad (58)$$

which is orders of magnitude below the other controllers. The force-feedback technique with low-frequency bypass opens the possibility for nanopositioning systems with a large range, wide bandwidth, and subatomic resolution. These characteristics are demonstrated experimentally in the following section.

The major penalty from eliminating the physical displacement sensor is that linearity is now dependent only on the piezoelectric force sensor and flexural spring constant  $k_f$ , which is less reliable. There is also no control of creep. Although these drawbacks may preclude the use of this technique in some applications, other applications, such as video-speed scanning probe microscopy [12]–[15], requiring subatomic resolution with a wide bandwidth will benefit greatly.

### F. Feedforward Inputs

The feedforward inputs  $u_{ff}$  shown in Fig. 11 can be used to improve the closed-loop response of the system [29]. Inversion-based feedforward provides the best performance, but the additional complexity is undesirable for the analog implementation considered in this study. A basic, but effective form of feedforward compensation is to simply use the inverse DC gain of the system as a feedforward injection filter, i.e.,

$$u_{ff} = k_{ff} r. \quad (59)$$

This is easily implemented and can provide a reduction in tracking lag.

With a feedforward input, the closed-loop transfer function of the dual-sensor and low-frequency bypass controller is

$$\widehat{G}_{dr} = \frac{k_{ff} G_{dVa} + G_{dVa} C_d}{1 + C_d G_{VsVa}}. \quad (60)$$

### G. Higher Order Modes

So far, only a single-degree-of-freedom system has been considered. Although this is appropriate for modeling the first resonance mode, it does not capture the higher order modes that occur in distributed mechanical systems. However, such higher order modes are not problematic, as they do not disturb the zero-pole ordering of the transfer function from the applied actuator voltage to the measured force.

In [42], it is shown that the transfer function of a generalized mechanical system with a discrete piezoelectric transducer and collocated force sensor is guaranteed to exhibit zero-pole ordering. That is, the transfer function  $G_{VsVa}$  will always exhibit zero-pole ordering. As the zero-pole ordering of the system is guaranteed, it follows that the controller discussed in Section III will also guarantee the stability of systems with multiple modes. The zero-pole ordering of an experimental system with multiple modes, and its successful control using the proposed technique, is reported in the following section.

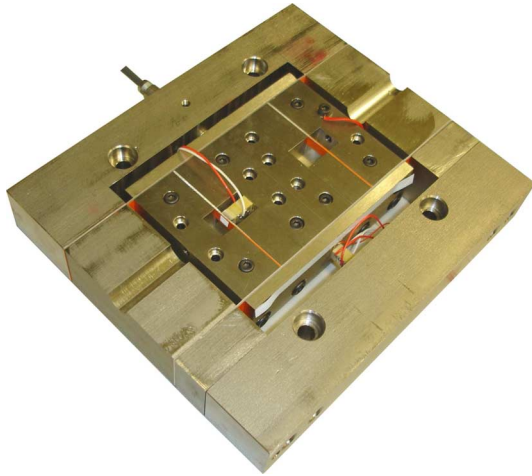


Fig. 12. High-speed nanopositioning platform described in [44].

## V. EXPERIMENTAL RESULTS

### A. Experimental Nanopositioner

In [44], a high-bandwidth lateral nanopositioning platform was designed by Kam K. Leang (University of Nevada, Reno) for video-speed scanning probe microscopy. This device, depicted in Fig. 12, is a serial kinematic device with two moving platforms both suspended by leaf flexures and driven directly by 10-mm stack actuators. The displacement is measured with an ADE Tech 2804 capacitive sensor.

The small stage at the center, designed for scan-rates up to 5 kHz, is sufficiently fast with a resonance frequency of 29 kHz [44]. However, the larger stage which provides motion in the adjacent axis is limited by a resonance frequency of 1.5 kHz. As this stage is required to operate with triangular trajectories up to 100 Hz, active control is required.

The main application for this nanopositioning device is high-speed scanning probe microscopy. In this application, high resolution and wide bandwidth are the most desirable characteristics. The force-feedback technique with low-frequency bypass, as discussed in Section IV-E, is the most suitable technique and will be applied here.

The platform under consideration is mechanically similar to the system shown in Fig. 1. The major difference is the existence of higher frequency modes beyond the first resonance frequency. These can be observed in the open-loop frequency response plotted in Fig. 15(a). Although only a single-mode system was previously discussed, the existence of higher order modes is not problematic. The zero-pole ordering and stability properties hold regardless of system order. This topic was discussed in detail in Section IV-G.

### B. Actuators and Force Sensors

As discussed in Section II-B, both piezoelectric plate and stack sensors can be used to measure force. A piezoelectric plate sensor is depicted in Fig. 13(a). Also shown in Fig. 13(b) is a 10-mm Noliac SCMAP07 actuator connected to a 2-mm Noliac CMAP06 stack force sensor. The metal half-ball is used

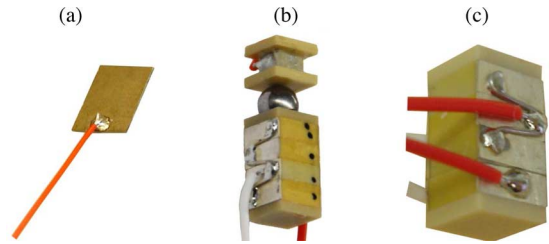


Fig. 13. Three types of piezoelectric force sensor: (a) a plate force sensor, (b) a stack actuator with discrete force sensor, and (c) a stack actuator with integrated force sensor.



Fig. 14. Piezodrive PDL200 voltage amplifier used to drive the actuator.

to eliminate the transmission of torsion and bending moments to the force sensor and moving platform.

For high-speed nanopositioning applications, the force sensor can also be integrated into the actuator. Such an arrangement is depicted in Fig. 13(c). The actuator is a standard 10-mm Noliac SCMAP07 stack actuator with one of the four internal actuators wired independently for use as a sensor.

Although integrated sensors are convenient and provide the highest mechanical stiffness, they also have an associated disadvantage. In addition to measuring the applied load force, an integrated sensor also detects contraction of the actuator due to the Poisson coupling as the actuator elongates. This contraction is coupled with the sensor and results in a small additive voltage that is opposite in polarity to the voltage induced by the load force. This error is small in systems where the flexural stiffness is appropriately matched to the stiffness of the actuator. In positioners with poorly matched actuators, i.e. where the flexural stiffness is much less than the actuator stiffness, the error due to the Poisson coupling can be significant. In such cases, however, the error can be eliminated using the arrangement shown in Fig. 13(b).

In the following experiments, the actuator with an integrated sensor is utilized. The integrated sensor simplifies the stage assembly and provides the highest mechanical stiffness.

The actuator was driven with a Piezodrive PDL200 linear amplifier shown in Fig. 14. With the 250 nF load capacitance, the PDL200 provides a bandwidth of approximately 30 kHz.

### C. Control Design

To facilitate analysis of the control loop, a model was procured using the frequency domain subspace technique<sup>2</sup> [45]. In

<sup>2</sup>A Matlab implementation of this algorithm is freely available from the author.

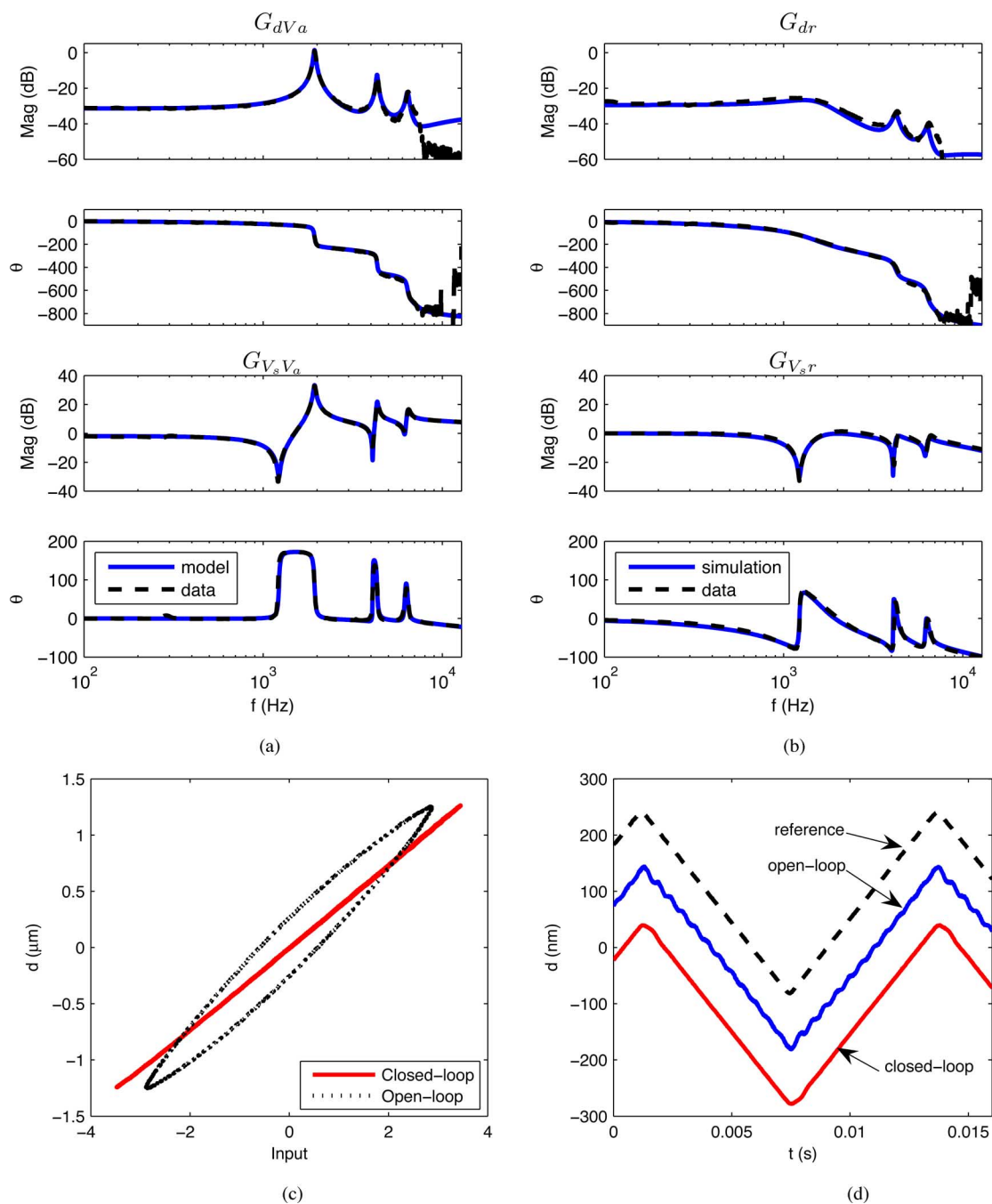


Fig. 15. The open- (a) and closed-loop (b) frequency responses of the nanopositioning system. Also plotted are the open- and closed-loop linearity (c) and response to an 80-Hz triangle wave (d). For the sake of clarity, the displacement curves in (d) have been offset from each other by 100 nm.

Fig. 15(a), the response of a seventh-order, single-input, two-output identified model can be verified to closely match the system response.

The optimal control gain was determined using the root-locus technique as  $\beta = 7800$ . Together with the 1-Hz corner frequency complementary filters, the controller was implemented with an analog circuit. Due to the simplicity of the control loop, analog implementation is straightforward and has the benefits of avoiding the quantization noise, finite resolution, and sampling delay associated with digital controllers.

The closed-loop frequency response is plotted in Fig. 15 and reveals significant damping of the first three modes by 24, 9, and 4 dB. In addition to experimental data, the simulated response is also overlain, which shows a close correlation. The tracking bandwidth of the closed-loop system is 2.07 kHz, which is higher than the open-loop resonance frequency and significantly greater than the bandwidth achievable with a direct tracking controller, predicted to be 210 Hz with a 5-dB gain margin.

In Fig. 15(c), the linearity of the system at 100 Hz is plotted. The large ellipse in the open-loop response is due solely to

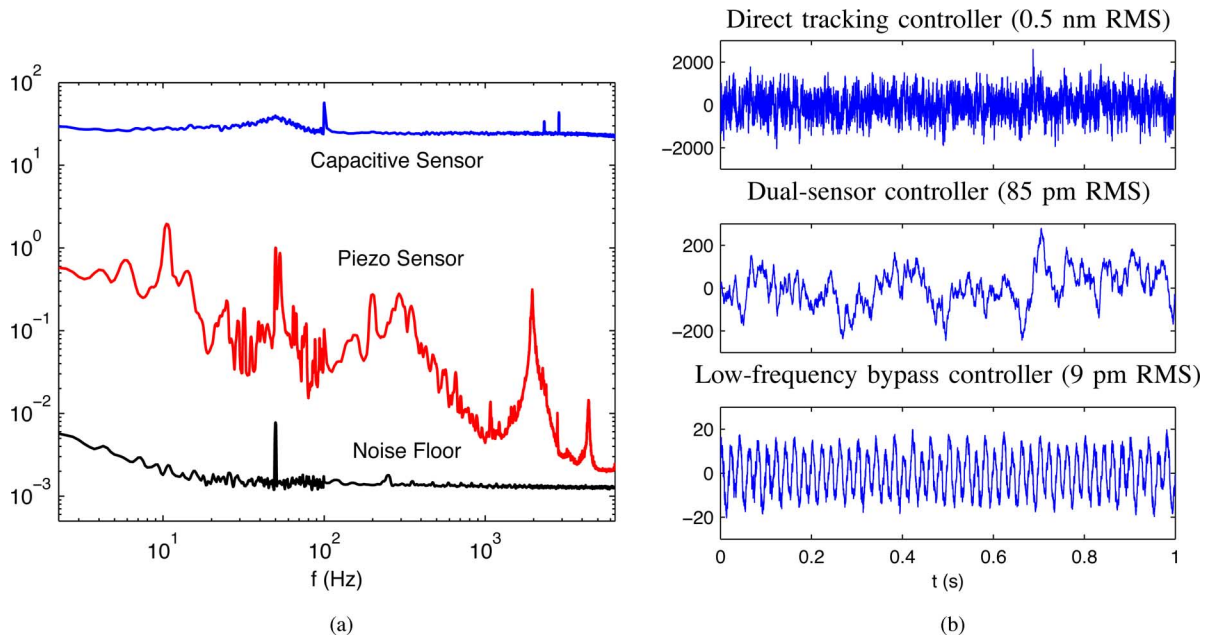


Fig. 16. (a) Power spectral density of the capacitive sensor, piezo transducer, and measuring instruments. (b) Closed-loop position noise of the controllers discussed in Section IV.

hysteresis as the system phase response at 100 Hz is negligible. Due to the high loop gain of the force-feedback controller, hysteresis is effectively eliminated, even at 100 Hz.

The time domain response of the closed-loop system to an 80 Hz triangular input is plotted in Fig. 15(d). Due to the high loop gain and resonance damping, the closed-loop response exhibits a negligible induced vibration and minimal tracking lag.

#### D. Noise Performance

A major benefit associated with the piezoelectric force sensor is the extremely low additive noise. To quantify the noise, it was necessary to amplify the sensor output by  $10^4$  using a circuit of the author's own design. The resulting signal magnitude is then large enough to analyze with an HP-35670A spectrum analyzer. Due to the stochastic nature of the signal, 1000 FFT averages were required to reduce the measurement variance to an acceptable level. The extremely low noise voltage produced by the piezoelectric sensor also necessitates the quantification of amplifier and instrumentation noise. This noise floor, which sets the limit of detection, was found to be approximately  $2 \text{ fm}/\sqrt{\text{Hz}}$ , which guarantees the statistical validity of the following measurements.

The power spectral densities of the capacitive and piezoelectric sensor noise, scaled to picometers per  $\sqrt{\text{Hz}}$  are compared in Fig. 16(a). At high frequencies, where the impedance of the piezoelectric transducer is low, the sensor noise is up to four orders of magnitude lower than the capacitive sensor noise, which is relatively independent of frequency at approximately  $26 \text{ pm}/\sqrt{\text{Hz}}$ . At lower frequencies, the improvement is more modest (see Section IV-A). However, even at 1 Hz, the piezoelectric sensor noise is only 2% of the capacitive sensor's noise,

which is  $29 \text{ pm}/\sqrt{\text{Hz}}$  compared to  $0.57 \text{ pm}/\sqrt{\text{Hz}}$ . In the time domain, the RMS noise of the capacitive sensor is 1.7 nm compared to 9.5 pm for the piezoelectric sensor.

In truth, the piezoelectric sensor noise is even lower than that shown in Fig. 16(a). The majority of measured noise power is actually due to external interference and mechanical excitation, not random noise. For example, the large peaks at 10 Hz and 2 kHz are due to mechanical and acoustic excitation of the mounting table and nanopositioner resonance. The large noise components at 50 Hz and between 150 and 500 Hz are also exogenous and most likely result from power-line frequency interference and harmonics arising from the use of fluorescent lighting. However, as these noise sources will likely be present in most practical applications, they are included in the following analysis.

The most intuitive method for evaluating closed-loop noise performance is to directly measure the sensor noise and simulate its effect on closed-loop position. The noise sensitivity transfer functions for the direct tracking controller, dual-sensor controller, and low-frequency bypass controller were discussed in Sections IV-C–IV-E. Based on a 1 s measurement of the capacitive and piezoelectric sensor noise, the resulting closed-loop position noise for each controller is plotted in Fig. 16(b). As expected, the direct tracking controller is noisiest as it uses the capacitive sensor signal over its entire closed-loop bandwidth. The dual-sensor controller provides an improved noise performance. However, the low-frequency bypass controller, which uses only the piezoelectric force sensor, has an exceptionally low closed-loop noise of only 9 pm RMS. The majority of this noise is clearly due to the 50 Hz interference. If this interference were eliminated with comprehensive shielding, the closed-loop position noise could potentially be reduced to just a few picometers.

It should be noted that this analysis has considered only *sensor-induced* noise. That is, the positioning noise resulting from the additive sensor noise. In practice, the magnitude of external disturbances will also have a significant impact on the overall positioning resolution, particularly if the sensor noise is reduced to the levels discussed here.

## VI. CONCLUSION

In this study, a force sensor is added to a nanopositioning stage. The resulting transfer function from the applied voltage to the measured force exhibits a zero-pole ordering which greatly simplifies the design and implementation of a damping controller.

In addition to damping control, the force sensor can also be used to estimate the platform displacement. This allows the damping controller to be adapted into an exceptionally high-performance tracking controller without sacrificing stability margins.

As with all piezoelectric sensors, the force sensor exhibits a high-pass characteristic at low frequencies. This problem is solved by replacing the low-frequency force signal with a physical displacement measurement or displacement estimate based on the open-loop system dynamics.

Simulations on a nanopositioner model demonstrate the effectiveness of the proposed tracking and damping controller. The dual-sensor IFF controller provides a closed-loop bandwidth approaching the open-loop resonance frequency while maintaining an infinite gain margin and  $90^\circ$  phase margin. By comparison, a standard integral displacement feedback controller achieves only 5% of the bandwidth with a gain margin of only 1 dB.

Future work involves the construction of a two-axis positioner with force feedback for video-speed atomic force microscopy.

## REFERENCES

- [1] S. Devasia, E. Eleftheriou, and S. O. R. Moheimani, "A survey of control issues in nanopositioning," *IEEE Trans. Control Syst. Technol.*, vol. 15, no. 5, pp. 802–823, Sep. 2007.
- [2] Z. Wang, L. Chen, and L. Sun, "An integrated parallel micromanipulator with flexure hinges for optical fiber alignment," in *Proc. IEEE Int. Conf. Mechatronics Autom.*, Harbin, China, Aug. 2007, pp. 2530–2534.
- [3] B. Potsaid, J. T. Wen, M. Unrath, D. Watt, and M. Alpay, "High performance motion tracking control for electronic manufacturing," *J. Dyn. Syst., Meas., Control*, vol. 129, pp. 767–776, Nov. 2007.
- [4] B. Bhushan, Ed., *The Handbook of Nanotechnology*. New York: Springer-Verlag, 2004.
- [5] S. M. Salapaka and M. V. Salapaka, "Scanning probe microscopy," *IEEE Control Syst. Mag.*, vol. 28, no. 2, pp. 65–83, Apr. 2008.
- [6] D. Y. Abramovitch, S. B. Andersson, L. Y. Pao, and G. Schitter, "A tutorial on the mechanisms, dynamics, and control of atomic force microscopes," in *Proc. Amer. Control Conf.*, New York, Jul. 2007, pp. 3488–3502.
- [7] E. Meyer, H. J. Hug, and R. Bennewitz, *Scanning Probe Microscopy. The Lab Tip*. Heidelberg, Germany: Springer-Verlag, 2004.
- [8] A. Ferreira and C. Mavroidis, "Virtual reality and haptics for nanorobotics," *IEEE Robot. Autom. Mag.*, vol. 13, no. 3, pp. 78–92, Sep. 2006.
- [9] A. A. Tseng, S. Jou, A. Notargiacomo, and T. P. Chen, "Recent developments in tip-based nanofabrication and its roadmap," *J. Nanosci. Nanotechnol.*, vol. 8, no. 5, pp. 2167–2186, May 2008.
- [10] A. A. Tseng, Ed., *Nanofabrication: Fundamentals and Applications*. Singapore: World Scientific, 2008.
- [11] H. C. Liaw, B. Shirinzadeh, and J. Smith, "Sliding-mode enhanced adaptive motion tracking control of piezoelectric actuation systems for micro/nano manipulation," *IEEE Trans. Control Syst. Technol.*, vol. 16, no. 4, pp. 826–833, Jul. 2008.
- [12] T. Ando, N. Kodera, T. Uchihashi, A. Miyagi, R. Nakakita, H. Yamashita, and K. Matada, "High-speed atomic force microscopy for capturing dynamic behavior of protein molecules at work," *e-J. Surface Sci. Nanotechnol.*, vol. 3, pp. 384–392, Dec. 2005.
- [13] G. Schitter, K. J. Åström, B. E. DeMartini, P. J. Thurner, K. L. Turner, and P. K. Hansma, "Design and modeling of a high-speed AFM-scanner," *IEEE Trans. Control Syst. Technol.*, vol. 15, no. 5, pp. 906–915, Sep. 2007.
- [14] A. D. L. Humphris, M. J. Miles, and J. K. Hobbs, "A mechanical microscope: High-speed atomic force microscopy," *Appl. Phys. Lett.*, vol. 86, pp. 034106-1–034106-3, 2005.
- [15] M. J. Rost, L. Crama, P. Schakel, E. van Tol, G. B. E. M. van Velzen-Williams, C. F. Overgaw, H. Ter Horst, H. Dekker, B. Okhuijsen, M. Seynen, A. Vijftigschild, P. Han, A. J. Katan, K. Schoots, R. Schumm, W. van Loo, T. H. Oosterkamp, and J. W. M. Frenken, "Scanning probe microscopes go video rate and beyond," *Rev. Sci. Instrum.*, vol. 76, no. 5, pp. 053710-1–053710-9, Apr. 2005.
- [16] A. J. Fleming and A. G. Wills, "Optimal periodic trajectories for band-limited systems," *IEEE Trans. Control Syst. Technol.*, vol. 13, no. 3, pp. 552–562, May 2009.
- [17] *The World of Micro- and Nanopositioning (PI Catalogue)*, Physike Instrumente (PI), Karlsruhe, Germany, 2005.
- [18] D. Y. Abramovitch, S. Hoen, and R. Workman, "Semi-automatic tuning of PID gains for atomic force microscopes," in *Proc. Amer. Control Conf.*, Seattle, WA, Jun. 2008, pp. 2684–2689.
- [19] A. J. Fleming, S. S. Aphale, and S. O. R. Moheimani, "A new method for robust damping and tracking control of scanning probe microscope positioning stages," *IEEE Trans. Nanotechnol.*, to be published.
- [20] S. S. Aphale, B. Bhikkaji, and S. O. R. Moheimani, "Minimizing scanning errors in piezoelectric stack-actuated nanopositioning platforms," *IEEE Trans. Nanotechnol.*, vol. 7, no. 1, pp. 79–90, Jan. 2008.
- [21] J. L. Fanson and T. K. Caughey, "Positive position feedback control for large space structures," *AIAA J.*, vol. 28, no. 4, pp. 717–724, 1990.
- [22] A. J. Fleming and S. O. R. Moheimani, "Sensorless vibration suppression and scan compensation for piezoelectric tube nanopositioners," *IEEE Trans. Control Syst. Technol.*, vol. 14, no. 1, pp. 33–44, Jan. 2006.
- [23] A. J. Fleming, S. Behrens, and S. O. R. Moheimani, "Optimization and implementation of multi-mode piezoelectric shunt damping systems," *IEEE/ASME Trans. Mechatronics*, vol. 7, no. 1, pp. 87–94, Mar. 2002.
- [24] A. Sebastian, A. Pantazi, S. O. R. Moheimani, H. Pozidis, and E. Eleftheriou, "A self servo writing scheme for a MEMS storage device with sub-nanometer precision," in *Proc. IFAC World Congr.*, Seoul, Korea, Jul. 2008, pp. 9241–9247.
- [25] S. S. Aphale, A. J. Fleming, and S. O. R. Moheimani, "Integral control of resonant systems with collocated sensor-actuator pairs," *IOP Smart Mater. Struct.*, vol. 16, pp. 439–446, Apr. 2007.
- [26] B. Bhikkaji and S. O. R. Moheimani, "Integral resonant control of a piezoelectric tube actuator for fast nanoscale positioning," *IEEE/ASME Trans. Mechatronics*, vol. 13, no. 5, pp. 530–537, Oct. 2008.
- [27] K. K. Leang and S. Devasia, "Feedback-linearized inverse feedforward for creep, hysteresis, and vibration compensation in AFM piezoactuators," *IEEE Trans. Control Syst. Technol.*, vol. 15, no. 5, pp. 927–935, Sep. 2007.
- [28] J. A. Butterworth, L. Y. Pao, and D. Y. Abramovitch, "A comparison of control architectures for atomic force microscopes," *Asian J. Control*, vol. 11, no. 2, pp. 175–181, Mar. 2009.
- [29] K. K. Leang, Q. Zou, and S. Devasia, "Feedforward control of piezoactuators in atomic force microscope systems," *Control Syst. Mag.*, vol. 29, no. 1, pp. 70–82, Feb. 2009.
- [30] W. T. Ang, P. K. Khosla, and C. N. Riviere, "Feedforward controller with inverse rate-dependent model for piezoelectric actuators in trajectory-tracking applications," *IEEE/ASME Trans. Mechatronics*, vol. 12, no. 2, pp. 134–142, Apr. 2007.
- [31] S. Devasia, "Should model-based inverse inputs be used as feedforward under plant uncertainty?" *IEEE Trans. Autom. Control*, vol. 47, no. 11, pp. 1865–1871, Nov. 2002.
- [32] K. Kim and Q. Zou, "Model-less inversion-based iterative control for output tracking: piezo actuator example," in *Proc. Amer. Control Conf.*, Seattle, WA, Jun. 2008, pp. 2710–2715.
- [33] Y. Li and J. Bechhoefer, "Feedforward control of a piezoelectric flexure stage for AFM," in *Proc. Amer. Control Conf.*, Seattle, WA, Jun. 2008, pp. 2703–2709.
- [34] S. Bashash and N. Jalili, "Robust adaptive control of coupled parallel piezo-flexural nanopositioning stages," *IEEE/ASME Trans. Mechatronics*, vol. 14, no. 1, pp. 11–20, Feb. 2009.
- [35] H. J. M. T. A. Adriaens, W. L. de Koning, and R. Banning, "Modeling piezoelectric actuators," *IEEE/ASME Trans. Mechatronics*, vol. 5, no. 4, pp. 331–341, Dec. 2000.

- [36] *IEEE Standard on Piezoelectricity*, ANSI/IEEE Standard 176–1987, 1988.
- [37] W. Q. Liu, Z. H. Feng, R. B. Liu, and J. Zhang, “The influence of preamplifiers on the piezoelectric sensor’s dynamic property,” *Rev. Sci. Instrum.*, vol. 78, no. 12, pp. 125107-1–125107-4, Dec. 2007.
- [38] P. Horowitz and W. Hill, *The Art of Electronics*. Cambridge, U.K.: Cambridge Univ. Press, 1989.
- [39] A. J. Fleming, A. G. Wills, and S. O. R. Moheimani, “Sensor fusion for improved control of piezoelectric tube scanners,” *IEEE Trans. Control Syst. Technol.*, vol. 15, no. 6, pp. 33–44, Nov. 2008.
- [40] A. Preumont, J. P. Dufour, and C. Malekian, “Active damping by a local force feedback with piezoelectric actuators,” *AIAA J. Guid. Control*, vol. 15, no. 2, pp. 390–395, 1992.
- [41] A. Preumont, *Mechatronics, Dynamics of Electromechanical and Piezoelectric Systems*. New York: Springer-Verlag, 2006.
- [42] A. Preumont, B. de Marneffe, A. Deraemaeker, and F. Bossens, “The damping of a truss structure with a piezoelectric transducer,” *Comput. Struct.*, vol. 86, pp. 227–239, 2007.
- [43] D. S. Nyce, *Linear Position Sensors. Theory and Application*. New York: Wiley, 2004.
- [44] K. K. Leang and A. J. Fleming, “High-speed serial-kinematic AFM scanner: Design and drive considerations,” *Asian J. Control*, vol. 11, no. 2, pp. 144–153, Mar. 2009.
- [45] T. McKelvey, H. Akcay, and L. Ljung, “Subspace based multivariable system identification from frequency response data,” *IEEE Trans. Autom. Control*, vol. 41, no. 7, pp. 960–978, Jul. 1996.



**Andrew J. Fleming** (S’02–M’03) was born in Dingwall, U.K., in 1977. He received the Bachelor of Electrical Engineering and Ph.D degrees from The University of Newcastle, Callaghan, Australia, in 2000 and 2004, respectively.

He is currently an Australian Research Council Fellow stationed at the School of Electrical Engineering and Computer Science, The University of Newcastle. He is the coauthor of two books, several patent applications, and more than 80 journal and conference papers. His current research interests include

nanopositioning, high-speed scanning probe microscopy, microcantilever sensors, and sensorless control of sound and vibration.

Dr. Fleming is an Associate Editor of *Advances in Acoustics and Vibration*. He was the recipient of The University of Newcastle Vice-Chancellor’s Award for Researcher of the Year in 2007. He was also the corecipient of the IEEE Control Systems Society Outstanding Paper Award for research published in the IEEE TRANSACTIONS ON CONTROL SYSTEMS TECHNOLOGY in 2007.